Walsh, K. J., Jawin, E., Barnouin, O., Bierhaus, E., Connolly, H., Molaro, J., McCoy, T., Delbo, M., Hartzell, C., Pajola, M., Schwartz, S., Trang, D., Asphaug, E., Becker, K., Beddingfield, C., Bennett, C., Bottke, W., Burke, K., Clark, B. (2019). Craters, boulders and regolith of (101955) Bennu indicative of an old and dynamic surface. *Nature Geoscience*, *12*(4), 242-246. https://doi.org/10.1038/s41561-019-0326-6

Peer reviewed version

Link to published version (if available):
10.1038/s41561-019-0326-6

Title: The Mature and Dynamic Surface of Bennu

Authors and affiliations: Kevin J. Walsh[1], Erica R. Jawin[2], Ronald-Louis Ballouz[3], Olivier S. Barnouin[4], Edward B. Bierhaus[5], Harold C. Connolly Jr.[6], Jamie L. Molaro[7], Tim McCoy[2], Dante S. Lauretta[3,] Marco Delbo[8], Christine Hartzell[9], Maurizio Pajola[10], Stephen R. Schwartz[3], David Trang[11], Erik Asphaug[3], Kris Becker[3], Chloe B. Beddingfield[12], William F. Bottke[1], Carina A. Bennett[3], Keara Burke[3], Benton C. Clark[13], Michael G. Daly[14], Dani DellaGuistina[3], Jason P. Dworkin[15], Catherine M. Elder[16], Dathon Golish[3], Alan R. Hildebrand[17], Renu Malhotra[3], John Marshall[12], Patrick Michel[8], Michael Nolan[3], Mark E. Perry[4], Bashar Rizk[3], Andy Ryan[8], Scott Sandford[18], Dan J. Scheeres[119], Hannah C. M. Susorney[20], Florian Thuillet[8],and the OSIRIS-REx Team.

[1]Southwest Research Institute, Boulder, CO, USA
[2]Smithsonian Institution National Museum of Natural History, Washington, DC, USA
[3]Lunar and Planetary Lab, University of Arizona, Tucson, AZ, USA
[4]The Applied Physics Laboratory, Johns Hopkins University, Laurel, MD, USA
[5]Lockheed Martin Space Systems Company, USA
[6]Department of Geology, School of Earth and Environment, Rowan University, Glassboro, NJ, USA
[7]Planetary Science Institute, Tucson, AZ, USA
[8]Université Côte d'Azur, Observatoire de la Côte d'Azur, CNRS, Laboratoire Lagrange, Nice, France
[9]Department of Aerospace Engineering, University of Maryland, College Park MD, USA
[10]INAF - Astronomical Observatory of Padova, Italy
[11]HIGP/University of Hawaii at Manoa, USA
[12]SETI Institute, Mountain View, CA, USA
[13]Space Science Institute, Boulder CO, USA
[14]Centre for Research in Earth and Space Science, York University, Toronto, ON, Canada
[15]NASA Goddard Space Flight Center, Greenbelt, MD, USA
[16]Jet Propulsion Laboratory, California Institute of Technology, Pasadena, CA, USA
[17]University of Calgary, Calgary, AB, Canada
[18]NASA Ames Research Center, CA, USA
[19]Dept. of Aerospace Engineering Sciences, University of Colorado, Boulder, CO, USA
[20]University of British Columbia, Vancouver, BC Canada

Small, kilometer-sized asteroids in the main belt are expected to have lifetimes of a few hundred million years before disruption via collision with another asteroid. Near-Earth asteroids (NEAs), which have evolved to their orbits from the main belt, are less likely to suffer impacts, but are still subject to possible re-shaping by the thermal YORP (Yarkovsky–O'Keefe–Radzievskii–Paddack) effect or tidal interactions with terrestrial planets. It is thus expected that their surfaces would be young and frequently refreshed. Here we show that early observations of NEA (101955) Bennu by the Origins, Spectral Interpretation, Resource Identification, and Security–Regolith Explorer (OSIRIS-REx) mission indicate a surface that is between 100 million and 1 billion years old, primarily through the measurement of numerous large candidate impact craters. We also observe many fractured boulders whose morphology suggests they have developed due to impact or thermal processes over a considerable amount of time since exposure at the surface. At the same time, the surface also shows signs of recent mass movement: clusters of boulders at topographic lows, a deficiency of small craters, and observed infill of existing large craters.

NASA's OSIRIS-REx asteroid sample return mission arrived at near-Earth asteroid (101955) Bennu on 3 December 2018 (Lauretta and DellaGuistina et al. 2019). An imaging campaign during the Approach phase (17 August to 2 December 2018) collected panchromatic images with the PolyCam imager (Rizk et al. 2018; DellaGiustina and Emery et al. 2019) at a range of phase angles and pixel scales, where the highest-resolution images were taken on 2 December from a range of 25 km. Images collected by the MapCam imager (Rizk et al. 2018) during the Preliminary Survey phase of the mission (3 to 19 December 2018) were combined with Approach-phase imaging to produce a 3D shape model of the asteroid, revealing a spheroidal shape with an equatorial ridge (Barnouin et al. 2019), as predicted by radar observations (Nolan et al. 2013).

Over the past three decades, ground-based and spacecraft observations of asteroids, combined with theoretical and computational advances, have transformed our understanding of small NEAs (diameters <~ 10 km). The combined lines of evidence have revealed that members of this population with diameters >~ 200 m are "rubble piles": gravitationally bound, unconsolidated fragments with very low bulk tensile strength (Richardson et al. 2002, Walsh et al. 2018). Asteroids in the main belt smaller than ~ 10 km are subject to Yarkovsky drift-induced ejection and collisional disruption on timescales shorter than the age of the Solar System. Thus, the current small asteroid population of the main belt is composed of reaccumulated remnants from collisions between larger asteroids (Michel et al. 2001). Previous *in situ* studies of the rubble-pile asteroid (25143) Itokawa found large boulders exposed on its surface, seemingly rapid degradation of impact craters, and evidence of substantial movement of surface material, suggesting an evolving surface that has undergone recent dynamical processing (Fujiwara et al. 2006, Miyamoto et al. 2007, Hirata et al. 2009).

The measured density and inferred high bulk porosity of Bennu (Scheeres et al. 2019, Barnouin et al. 2019), and the lack of either high surface slopes or substantial topographic relief indicate that Bennu is a rubble pile. Bennu's volume as established by its shape, combined with its mass measured during Preliminary Survey flybys (Scheeres et al. 2019), determine a density of 1189 kg/m^3. This density would require 25–50% bulk porosity if it is constructed primarily of CI (bulk density of 1570 kg m^{-3}) or CM (bulk density of 2200 kg m^{-3}) chondrite–like material (Hamilton et al. 2019). If the microporosity present in these meteorite classes is also considered (Macke et al. 2011), the total porosity of Bennu may be as high as 70%. In addition, the slope at each point on the surface of Bennu—determined from the combination of the shape, mass, and spin state—shows a relaxed distribution with values averaging ~17° for the highest resolution shape model, and almost entirely below typical angles of ~30° allowed by the angle of repose of terrestrial materials (Scheeres et al. 2019).

The largest boulders have the greatest local relative topographic relief on the surface of Bennu, some with heights >20 m (Figure 1a). One of the largest boulders on Bennu was first detected with ground-based radar and estimated to be 10 to 20 m in diameter (Nolan et al. 2013). This same boulder was detected in Approach phase imaging and measured to be 55m in diameter (Figure 1a.), and this imaging campaign identified at least three boulders with long axes exceeding 40m and more than 20 boulders larger than 20m (DellaGuistina et al. 2019). Objects of this size are larger than plausible crater ejecta from any of the large crater candidates on Bennu (Bart and Melosh 2007), suggesting instead that their origins trace back to the formation of Bennu or earlier. The possible inherited origin of Bennu's largest boulders supports the idea that rubble piles form as reaccumulated remnants of disruptive collisions of larger asteroids in the main asteroid belt (Michel et al. 2001).

Boulders on Bennu display albedo and color diversity (DellaGuistina and Emery et al. 2019), with some showing these differences within distinct meter-sized clasts in an otherwise unfragmented rock. We interpret such assemblages as impact breccias (Figure 1b). Processes capable of creating breccias spanning tens of meters with meter-sized clasts imply energetic events that far exceed what Bennu can support (Bischoff et al. 2006). Thus, the existence of breccias requires that they formed in a parent-body generation of Bennu, possibly related to the catastrophic disruption event that formed Bennu, or they are a record of the parent body's accretion. The noted albedo and color diversity of the largest boulders, and the distinct meter-scale components visible in some of them, may point to the compositional diversity of Bennu's parent body and its catastrophic impactor or diversity within the parent body itself.

The boulders on Bennu's surface also exhibit a diversity of sizes, geologic context, and morphologies. To date, boulders > 8m in diameter have been adequately resolved with

PolyCam images, for which we have measured a size-frequency distribution best fit with a power-law index of –2.9 ± 0.3 (DellaGiustina and Emery et al. 2019). Many of these boulders appear to be resting on top of the surface, while some are partially buried, pointing to either active burial and/or exhumation processes. Several examples of imbricated boulders have been identified, although these locations are smaller in extent than the imbricated regions that were observed on Itokawa (Miyamoto et al., 2007) with no obvious correlation between imbrication and fine-grained deposits. Both rounded and angular boulders are present on the surface, which may suggest a variety of formation mechanisms, compositions, and/or boulder evolutionary processes.

We readily observe fractured boulders over the surface exhibiting multiple fracture types. Some of the most dramatic examples include large, linear fractures that appear to split boulders into two or more pieces. These occur at all resolvable scales and within some of the largest boulders on the surface. In contrast, other boulders exhibit non-linear fractures that suggest some interaction between the fracture-driving mechanisms and the rock bulk structure. We also found examples of discrete, yet tightly clustered meter-scale boulders that appear to have fractured *in situ*, and remain in clusters with minimal displacement (Lauretta and DellaGuistina et al. 2019). Complex networks of fractures also occur in some boulders (Fig. 1c, 1d), with many deep fractures crossing each other at various angles, although some are clearly linear. These numerous and morphologically varied fractures may be produced by one or a combination of processes, such as large-scale impact events, micrometeoroid impacts, and thermal fatigue. The latter two processes may also be responsible for the shallow fractures and surficial features observed on visibly textured boulders, which indicate exfoliation, near-surface disaggregation, or regolith production processes [e.g., Molaro et al. 2017; Delbo et al. 2014; Basilevsky et al., 2015].

Although boulder fracture could potentially represent artifacts of past processing on Bennu's parent-body, the abundance of fractured boulders and some cases where boulders appear to have disaggregated *in situ* points to surface processes active in Bennu's recent geologic history, since it evolved to a near-Earth orbit. On the other hand, these fracture formation mechanisms need time to occur, suggesting that the surface has not been dynamically refreshed since Bennu's transition from the main belt to its near-Earth orbit, where a typical near-Earth asteroid's dynamical lifetime is on order 10Myr (Gladman et al. 2000). Breakdown due to micrometeorite bombardment and thermal fatigue is predicted to be faster and slower, respectively, in the main belt than in near-Earth space [Graves et al., 2019; Molaro et al., 2017; Basilevsky et al., 2015]. However, the relative efficiencies of these and other active processes are not well constrained, making it difficult to use fractures to assess the absolute surface age. Some processes also act over multiple timescales, such as thermal fatigue, which may generate fractures over different spatial scales owing to diurnal and annual thermal cycles.

We find concentrations of boulders in local topographic lows (with tens of meters topographic differences), with boulder abundances up to an order of magnitude greater than the global average (Figure 2). The boulders in topographic lows are often bounded by linear ridges. Using images and derived global digital terrain models (DTMs), we identified several of these linear structures across Bennu (Barnouin et al. 2019), and the majority contain concentrations of boulders. Bennu has several different types of linear features including north-south–oriented ridges spanning lengths from 80 to 330 m, with the longest extending from the north pole to the equator. The widths of these features vary from 2 to 30 m, and they possess geometric heights of 1 to 5 m relative to the surrounding terrain and contribute to the non-circularity of the equator (Barnouin et al. 2019). They are most prominent in the +Z (northern) hemisphere (Figure 2), though there are smaller features similar to grooves or scarps with different orientations in both hemispheres (Barnouin et al. 2019).

Bennu has experienced a number of impacts that have transformed its surface. We have identified several tens of candidate impact craters, which range in size from ~10 m to >150 m in diameter. The characteristics of distinct candidate impact craters include circular features with raised rims and depressed floors, and/or clear textural differences (apparent concentration or lack of boulders) between the interior and exterior of the crater. Less distinct candidate craters have subdued rims or an absence of raised rims, shallow interiors, and lack of contrast between the interior and exterior boulder populations. Based on current image data, we have identified 12 distinct, and at least 40 less distinct, candidate craters. Notably, several large distinct craters are located on Bennu's equatorial ridge, suggesting that the ridge is a stratigraphically old feature (Figure 3).

We used the population of large distinct candidate craters (D > 50m) to estimate the age of Bennu's surface. Assuming that the craters record impact events, they are primarily a record of Bennu's history in Main Belt (Bottke et al. 2005). Crater scaling laws can convert impact parameters to crater diameters, although for small rubble-pile bodies there is added uncertainty due to their microgravity regime (Holsapple 1993, 2007). Considering the expected collisional frequency and distribution of asteroid sizes in the main belt (Bottke et al. 2005), it would take 100 million to 1 billion years to explain the creation of Bennu's largest crater candidates (Figure 3d). However, cratering into lower-strength material under low-gravity conditions can lead to enhanced crater diameters, which could reduce age estimates (Holsapple 2007). Meanwhile, cratering into high-porosity material may lead to reduced diameters and older ages (Prieur et al. 2017). Dating the surface exposure age of the returned sample will reduce the uncertainty in surface age and provide a better understanding of which aspects play dominant roles in crater formation on Bennu and other high-porosity, low-strength targets.

The imaging and topographic data allowed identification of craters ~10 m and larger. The observations show a depletion of small craters (~10 m < D < 50 m) relative to expectations

based on the production rate of large craters (Figure 3d). The depletion of small craters has also been found on other NEAs including Itokawa and Eros (Thomas and Robinson et al. 2005; Michel et al. 2009). The prevalence of boulders on the surface can potentially frustrate the formation of small craters, whereby impactors strike and break boulders rather than making craters (Tatsumi et al. 2017). Conversely, the depletion of small craters may reflect, as previously postulated, crater erasure due to surface material movement and/or seismic shaking (Richardson et al. 2005, Asphaug 2008), and there are clear examples on some large candidate craters on Bennu of material movement and crater infill (Figure 4).

The interiors of many small candidate impact craters (D < 20 m) are largely devoid of resolvable boulders (Figure 3). These locations may be reservoirs for smaller particles produced or exposed during the crater formation process, while boulder fracturing processes or abrasion/mechanical erosion between boulders could both contribute to the production of fine grains more widely across the surface of Bennu. The evidence for fine-grained material (of the centimeter-scale sizes that are ingestible by the OSIRIS-REx sample mechanism [Bierhaus et al. 2018] and of smaller, micron-scale sizes) is abundant despite not being resolved with current imaging. The measured thermal inertia suggests a substantial population of centimeter-sized particles (DellaGuistina and Emery et al. 2019). The phase reddening observed with the MapCam images suggest some photometric contribution by micron-sized particles (DellaGuistina and Emery et al. 2019). Thermal emission spectra (Hamilton et al. 2019) are consistent with a surface that may comprise a mixture of particle sizes from centimeters or greater down to tens of microns. Finally, a few regions only a few meters in size have large albedo differences and lack observable particles that suggest ponding or mantling by distinctly lower-albedo material (Lauretta and DellaGuistina et al. 2019). These dark patches appear as surficial layers indiscriminately draped over boulder and inter-boulder areas alike (see DellaGuistina and Emery et al. 2019). However, low-albedo deposits do not mask the outlines of boulders. The dark material comprising these patches may be composed of dust or fine particles.

Finding and collecting small particles is the goal of the OSIRIS-REx mission, and the Approach and Preliminary survey mission phases have provided images to build a geologic assessment of Bennu that will be valuable for providing context of the returned sample. The retention of large craters on Bennu's equatorial ridge requires that the surface age predates the expected ~10-million-year duration as a near-Earth asteroid. Bennu's surface therefore also recorded processes from its time in the main belt; the formation timescales of the largest craters suggest that Bennu recorded hundreds of millions of years of history during this period. The large boulders on its surface trace back even farther in time and may provide information about the composition and geology of its parent body, as well as the collision that disrupted it. Finally, the observed impact breccias may have formed during the evolution of its parent body, through repeated impact events on its surface over most of solar system history, or during the large impact event that resulted in the formation of

Bennu. Alternatively, these breccias may even date to the accretion time of its parent body in the protoplanetary disk. Within the disk, the parent may have formed beyond Jupiter's orbit, where it grew by way of meter-sized "pebbles" that drifted through the disk (Kretke and Levinson, 2015). Here those building-block pebbles are revealed as the similarly-sized constituents of some of the observed breccias, similar in sizes to textures observed on comet 67P/Churyumov-Gerasimenko (Davidsson et al. 2016). This would imply that Bennu's parent body formed in the outer solar system, where meter-sized pebbles would have been accessible, and was later implanted or delivered into the main belt (Warren 2011; Kruijer et al. 2017).

References

Asphaug, E. Critical crater diameter and asteroid impact seismology. Meteoritics and Planetary *Science* **43**, 1075-1084 (2008).

Barnouin O. S. et al. this issue (2019).

Bart, G. D., Melosh, H. J., Using lunar boulders to distinguish primary from distant secondary impact craters. *Geophysical Res. Lett.,* **34**, L07203, (2007).

Basilevsky, A.T., Head, J.W. and Horz, F., Survival times of meter-sized boulders on the surface of the Moon. *Planetary and Space Sci.*, **89**, 118-126, (2013).

Basilevsky, A. T., Head, J. W., Horz, F., Ramsley, K., Survival times of meter-sized rock boulders on the surface of airless bodies. *Planetary and Space Sci*. **117**, 312-328, (2015).

Bierhaus, E. B., Clark, B. C., Harris, J. W., et al., The OSIRIS-REx Spacecraft and the Touch-and-GoSample Acquisition Mechanism (TAGSAM). *Space Sci. Rev.*, **214**, 107, (2018).

Bischoff, Addi, Edward RD Scott, Knut Metzler, and Cyrena A. Goodrich. in *Meteorites and the early solar system II* (eds. D. S. Lauretta and H. Y. McSween Jr.) 679-712 (University of Arizona Press, Tucson, AZ, 2006).

Bottke, W. F., Durda, D. D., Nesvorny, D., Jedicke, R., Morbidelli, A., Vokrouhlicky, D., Levison, H. 2005. The fossilized size distribution of the main asteroid belt. *Icarus* **175**, 111-140, (2005).

Davidsson et al., The primordial nucleus of comet 67P/Churyumov-Gerasimenko. Astron. & Astrophysics **592,** A63, (2016).

Delbo, M., Libourel, G., Wilkerson, J., Murdoch, N., Michel, P., Ramesh, K. T., Ganino, C., Verati, C., Marchi, S., Thermal fatigue as the origin of regolith on small asteroids. *Nature* **508**, 233-236, (2014).

DellaGuistina D. and Emery J. et al. this issue (2019).

Fujiwara, A., Kawaguchi, J., Yeomans, D. K., et al., The Rubble-Pile Asteroid Itokawa as Observed by Hayabusa, *Science*, **312**, 1330, (2006).

Gladman B, Michel P, Froeschle´ C.. The Near-Earth Object Population, *Icarus* **146**, 176–89 (2000).

Graves, K. J., D. A. Minton, J. L. Molaro, M. Hirabayashi, Resurfacing Asteroids from Thermally Induced Surface Degradation. *Icarus*, 322, 1-12 (2019).

Hamilton V. et al. this issue (2019).

Hirata, N., Barnouin-Jha, O. S., Honda, C., et al., A survey of possible impact structures on 25143 Itokawa, *Icarus*, **200**, 486, (2009).

Holsapple, K. A., *Ann. Rev. Earth Planet. Sci.,* **21**, 333, (1993).

Lauretta D. S. and DellaGuistina D., et al. this issue (2019).

Macke, Robert J., Guy J. Consolmagno, and Daniel T. Britt. Density, porosity, and magnetic susceptibility of carbonaceous chondrites. *Meteoritics & Planet. Sci.* **46**, 1842-1862, (2011).

Molaro, J.L., Byrne, S. and Le, J.L., Thermally induced stresses in boulders on airless body surfaces, and implications for rock breakdown. *Icarus*, **294**, 247-261, (2017).

Michel P, Benz W, Tanga P, Richardson DC. Collisions and gravitational reaccumulation: Forming asteroid families and satellites. *Science,* **294***,* 1696–1700, (2001).

Michel, P., O'Brien, D.P., Abe, S., Hirata, N. Itokawa's cratering record as observed by Hayabusa: implications for its age and collisional history. *Icarus* **200**, 503-513, (2009).

Miyamoto H. et al. Regolith migration and sorting on asteroid Itokawa, *Science* **316***,* 1011–1014 (2007).

Nolan MC, Magri C, Howell ES, Benner LAM, Giorgini JD, et al. Shape model and surface properties of the OSIRIS-REx target Asteroid (101955) Bennu from radar and lightcurve observations. *Icarus* **226**, 629-640, (2013).

Kretke, K. A., & Levison, H. F. Evidence for pebbles in comets, *Icarus*, **262**, 9, (2015).

Kruijer, T. S., Burkhardt, C., Budde, G., & Kleine, T. Age of Jupiter inferred from the distinct genetics and formation times of meteorites, *Publ. Nat. Acad. Sci.* , **114**, 6712, (2017).

Prieur, N. C., T. Rolf, R. Luther, K. Wünnemann, Z. Xiao, S. C. Werner The effect of target properties on transient crater scaling for simple craters, *JGR: Planets*, **122**, 1704-1726, (2017).

Richardson, D. C., Leinhardt, Z. M., Melosh, H. J., Bottke, W. F. & Asphaug, E. in Asteroids III (eds Bottke, W. F. Jr, Cellino, A., Paolicchi, P. & Binzel, R. P.) 501–515 (Univ. of Arizona Press, Tucson, AZ, 2002).

Richardson, J. E., Melosh, H. J., Greenberg, R. J., O'Brien, D. P. The global effects of impact-induced seismic activity on fractured asteroid surface morphology. *Icarus* **179**, 325-349 (2005).

Rizk, B., et al. OCAMS: the OSIRIS-REx camera suite. *Space Sci. Rev.*, **214**, 26 (2018)

Scheeres D. J. et al. this issue (2019).

Tatsumi, E. & Sugita, S. Cratering efficiency on coarse-grain targets: Implications for the dynamical evolution of asteroid 25143 Itokawa. *Icarus,* **300**, 227-248 (2017).

Thomas, P. C. & Robinson, M. S. Seismic resurfacing by a single impact on the asteroid 433 Eros. *Nature* **436**, 366-369 (2005).

Walsh, K. J. Rubble Pile Asteroids. Annu. Rev. Astron. Astrophys. **56**, 593-624 (2018).

Warren, P. H., Stable-isotopic anomalies and the accretionary assemblage of the Earth and Mars: A subordinate role for carbonaceous chondrites. Earth and Planetary Science Letters, **311**, 93, (2011).

Corresponding Author: Kevin Walsh (kwalsh@boulder.swri.edu)

Acknowledgements

This material is based upon work supported by NASA under Contract NNM10AA11C issued through the New Frontiers Program. M. Pajola was supported for this research by the Italian Space Agency (ASI) under the ASI-INAF agreement no. 2017-37-H.0. Delbo, Michel and Ryan would like to acknowledge the French space agency CNES. M.D., A.R., P.M. and S.R.S acknowledge support from

the Academies of Excellence on Complex Systems and Space, Environment, Risk and Resilience of the Initiative d'EXcellence "Joint, Excellent, and Dynamic Initiative" (IDEX JEDI) of the Université Côte d'Azur.

Author contributions

K.J.W. led the mapping, analysis and manuscript writing, E.R.J, R-L.B, O.S.B, E.B.B, H.C.C., J.L.M, T.M contributed to the mapping, analysis and writing of the manuscript. D.S.L leads the mission and contributed to analysis and writing. M. D., C. H., M.P., S.R.S., and D.T. contributed to mapping and manuscript writing. E. A., K. B., C. B. B., W. F. B., C. A. B., K. B., B. C. C., M. G. D., D. D., C. M. E., D. G., A. R. H., J. M., P. M., M. N., M. E. P., B. R., A. R., D. J. S., H. C.C., M. S., F. T all contributed to the mapping, analysis or manuscript writing.

Author information

(basically affiliations)

Main figure legends

Figure 1: **The boulders of Bennu can be large and are sometimes fractured or brecciated**.
(a) A boulder with diameter of ~50 m and height of over 20 m relative to the surrounding the surface of Bennu.
(b) A brecciated boulder that is ~21 m in diameter with 3- to 4-m constituent pieces showing measurable geometric albedo differences, ranging from 3.7 to 5.0%.
(c) A ~40-m boulder that shows a complex web of large fractures.
(d) A ~20-m boulder with a single linear fracture.
(e) Boulder abundance map of the surface of Bennu based on a 49,152-facet shape model of the surface, where the boulder abundance is calculated by counting the number of boulders within a radius of 25 m in each facet and then normalized to square kilometer.
Image for (a) is ocams20181201t055746s307_pol_iofl2pan_63551 taken 1-December-2018 from a spacecraft distance of 31.5km, (b) and (d) taken from image ocams20181202t072303s706_pol_iofl2pan_63785 taken 02-Dec-2018 with a spacecraft distance 24.0 km, and (c) taken from image ocams20181202t082747s619_pol_iofl2pan_63714 taken 02-Dec-2018 with a spacecraft distance of 23.8 km.

Figure 2: Ridges in the northern hemisphere on Bennu define regions of high boulder abundance. Image ocams20181201t065147s197_pol_iofl2pan_63482 taken 01-Dec-2018 from a spacecraft distance of 31.3 km is projected onto the shape model with colored shaded relief. Cyan lines indicate the locations of several ridges. The depressed region between the ridges contains a high concentration of boulders relative to the surrounding terrain. Numerous impact crater candidates are also visible in the equatorial regions.

Figure 3: The craters of Bennu. (a) An example feature of Bennu's surface that meets all of the criteria to be considered as a distinct candidate crater, including clear topography

associated with its rim. This equatorial crater is centered 3 deg below the equator and has a diameter of 81m. (b) A distinct crater with diameter of 44m shows a textural difference inside and outside of its rim and a distinct lack of boulders (c) Example of a less distinct candidate crater with some textural differences between the inside and outside of the circular feature but that shows only hints of being a circular feature with no clear topography. (d) The established "distinct" candidate craters provide a lower bound on age by comparing their distributions to the expected crater production function (see Methods), and we use the entire population of less distinct candidate craters to estimate an upper bound. In both groups, the change in size-frequency distribution appears around D = 50 km. Image ocams20181202t083822s735_pol_iofl2pan_64172 was used for (a) and (b) and was taken 02-Dec-2018 from a spacecraft range of 23.7 km. Image for (c) was ocams20181202t091159s321_pol_iofl2pan_64104 and was taken 02-Dec-2018 from a spacecraft range of 23.5km.

Figure 4: **Flow of material into a D=160m candidate crater**. (a) A large candidate crater is centered near the equator and initial measurements find a diameter of 160m. Three circles are illustrated with (red) D=160m, (navy) D=100m and (aqua) D=50m, and represent the center of 5m wide annulus that is used to analyze the elevation profiles azimuthally. (b) The elevation at each point of the DTM are extracted azimuthally along each of the three drawn circles and plotted as a function of angle counter-clockwise from East. The outer annulus tracks the candidate crater rim and shows roughly a ~10m height above the middle and inner annuli. All three show the similar profile of increased height between angles ~180-280 which is the region indicated with gray background. (c) Image showing the relationship between the material flow and the candidate crater. White arrows indicate the crater rim, while yellow arrows indicate the edge of the flow which has entered the crater from the west (the flow correlates with the elevated portion of the topographic profile). Stratigraphic relationships show that the flow occurred after the formation of the crater. Leftmost yellow arrow indicates additional material movement that has partly buried the westernmost portion of a larger boulder. Image ocams20181201t051455s588_pol_iofl2pan_63071 was used for (c) and was taken 1-Dec-2018 from a spacecraft distance of 31.820613 km.

Methods:

Initial boulder identification was carried out following the methods outlined in (DellaGiustina et al., 2019). Subsequent detailed mapping and geologic analyses of boulders were performed by a visual analysis of PolyCam and MapCam data using the Small Body Mapping Tool (SBMT), which projects spacecraft images onto a shape model (Ernst et al., 2018). Boulders were mapped by drawing an ellipse around the resolved boulder margins; this method allows for the analysis of both long and intermediate axis lengths, as well as boulder orientation. Boulders were viewed under a range of viewing geometries including various phase angles and illumination angles. Detailed boulder morphology was assessed using a combination of unprojected images which facilitated fine-scale analyses, and projected images within SBMT, which provides geologic context. Boulder abundance (Fig 1e) was calculated using a 49,152-facet shape model of the surface, where the boulder abundance was calculated by counting

the number of boulders within a 25 m radius in each facet and then normalizing to 1 square kilometer.

Crater identification and measurement was performed using a combination of projected and unprojected PolyCam and MapCam images, as well as SPC-derived topography data (Barnouin et al. 2019). All mapping was carried out in SBMT by mapping ellipses around the maximum extent of the resolvable crater rim. Multiple members of the team mapped the surface for craters and only those mapped by multiple members as distinct crater candidates were counted in the "distinct" category for the purposes of analysis. All mapped individual craters were included in the "non-distinct" group. To calculate surface age, we used the largest craters to estimate a range of possible surface ages based on the impactor size distribution found in the main belt, an average main-belt impact probability and impact velocity (P_{imp} = $2.86x10^{-18}$ km^{-2} yr^{-1} and v_{imp} = 5.3 km/s) (Marchis et al. 2010, Bottke et al. 2005), and a crater scaling law for dry soil with a strength of 0.18 MPa (Holsapple 1993). The clearly established "distinct" candidate craters provide a lower bound on age, and we use the entire population of less distinct candidate craters to estimate an upper bound. In both groups, the change in size-frequency distribution appears around D = 50 km.

Linear features were mapped within SBMT by a visual assessment of the SPC-derived shape model at a variety of shape model resolutions. Where linear features were apparent in the shape model, a combination of projected and unprojected PolyCam and MapCam images were assessed for evidence of the same linear feature. Images used for this analysis included a range of viewing geometries to minimized the possibility of a false detection due to shadows cast from boulders.

Many of the geologic assessments relied on elevation, which was derived from the shape model. The construction of the shape model and calculation of elevation is described in detail in other works (Barnouin et al. 2019).

Data availability. [raw through calibrated datasets] will be available via the Small Bodies Node of the Planetary Data System (https://pds-smallbodies.astro.umd.edu/) [add when if known]. [higher-level products, e.g., shape models, DTMs] will be available in the Planetary Data System 1 year after departure from the asteroid."

Additional references only in the Methods

They use the same formatting of the main text references. Please remember *not* to start the numeration from [1] again.

Ernst, C. M., Barnouin, O. S., Daly, R. T., The Small Body Mapping Tool (SBMT) for Accessing, Visualizing, and Analyzing Spacecraft Data in Three Dimensions, LPSC 49, abstract no. 1043 (2018).

Marchi et al., The cratering history of (2867) Steins. Planetary and Space Science, Volume **58**, 1116-1123 (2010).

Figures

Figure 1: [Pane e to be flipped with the better color scale -pasted below]

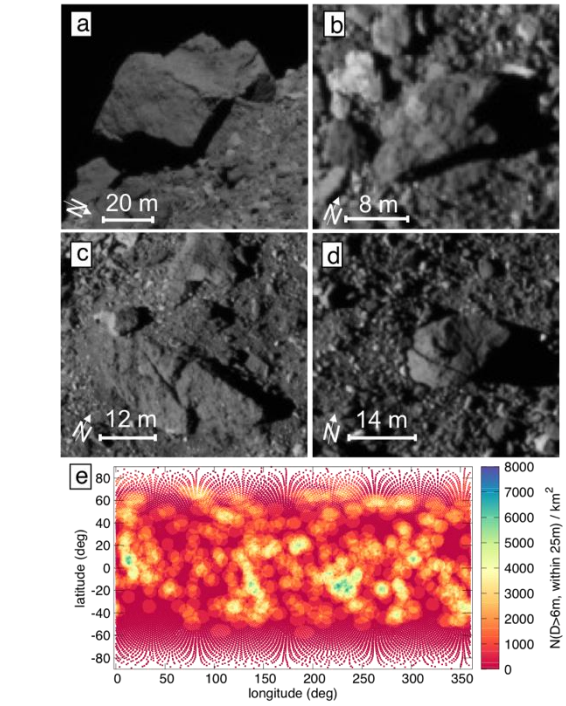

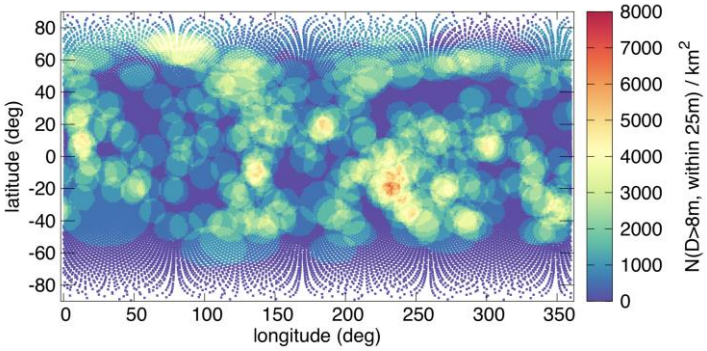

Figure 2:

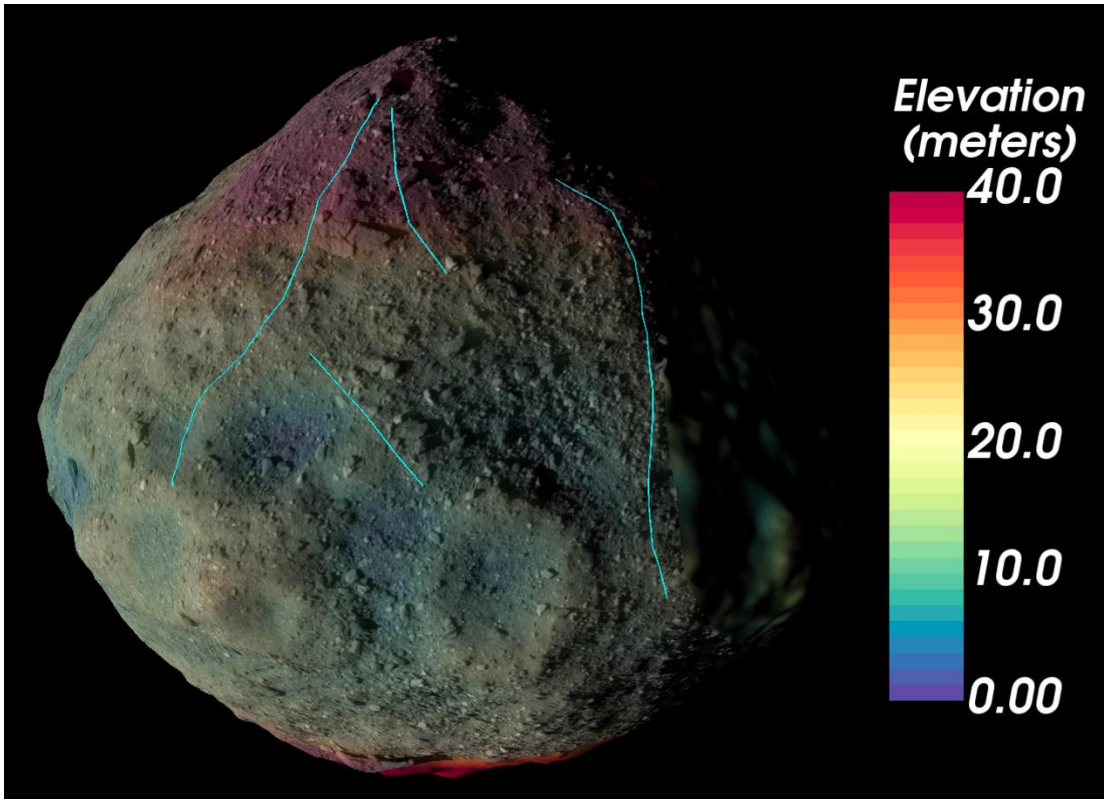

Figure 3: **[KJW has a replacement for pane d also, with new Ruby diameter and v_av=5.3km/s]**

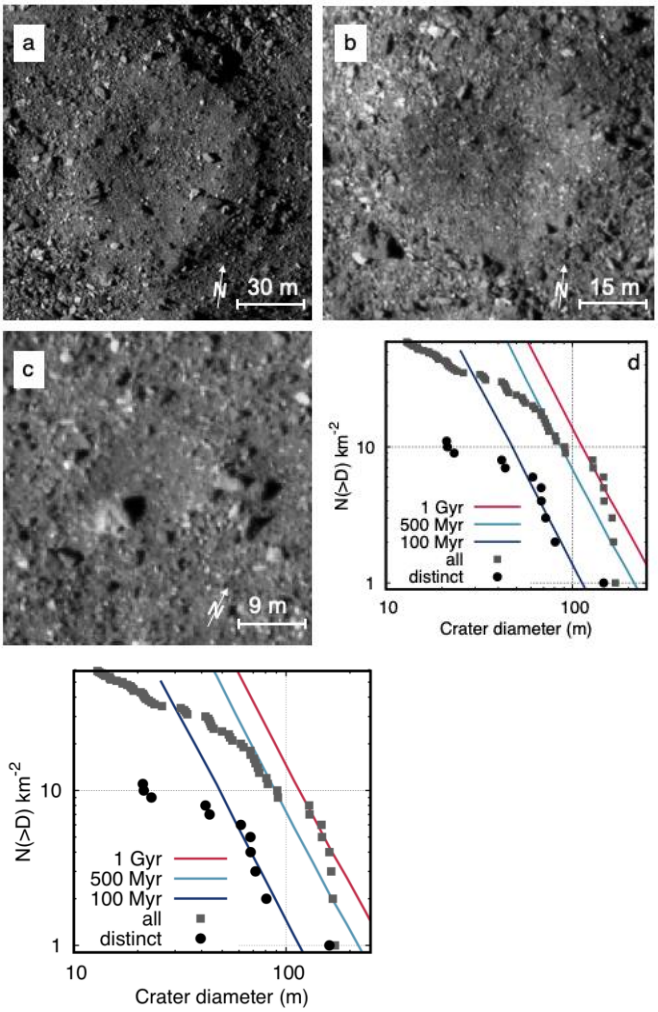

Figure 4: [Replacement for pane a is pasted below] [KJW should draw out the region from 180-280 on pane a plot]

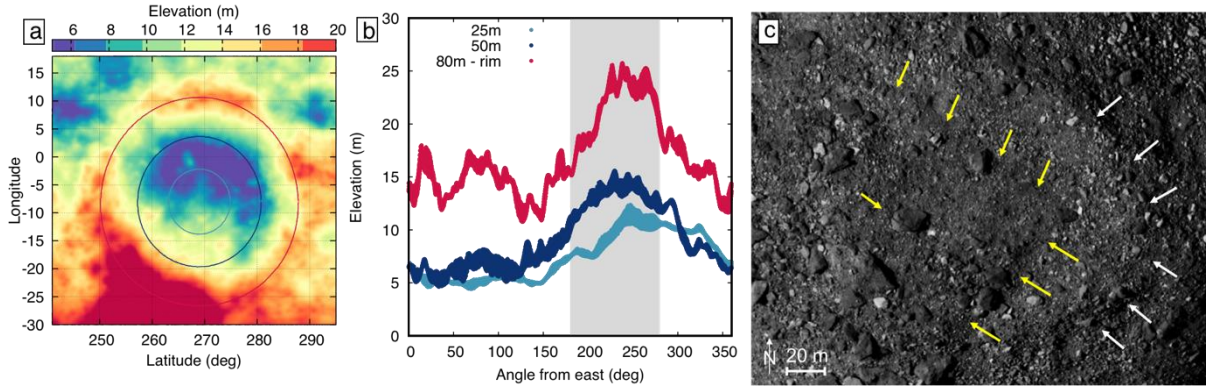

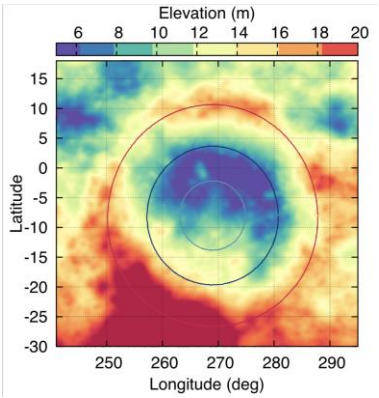

As mentioned above, the figures should be submitted separately, at least for the final version of the paper.

Very important note Choosing the right electronic format for your figures will be essential for speeding up the processing of your paper. See the detailed art guidelines here: www.nature.com/documents/NRJs-guide-to-preparing-final-artwork.pdf .
The main message is that we accept vector figure types (EPS, PDF, AI) with the appropriate resolution, whereas we might have problems with raster figures (PNG, JPG).
We might edit your figures/tables electronically so they conform to Nature style. If necessary, we will re-size figures to fit single or double column width.
If your figures contain several panels, they should be labelled lower case (a), (b), and so on, and form a neat rectangle when assembled. Use these letters to refer to them in the captions (rather than "top left", "the rightmost panel", and the like)

Should your paper contain any items (figures, tables, images, videos or text boxes) that are the same as (or are adaptations of) items that have previously been published elsewhere and/or are owned by a third party, please note that it is your responsibility to obtain the right to use such items and to give proper attribution to the copyright holder. This includes pictures taken by professional photographers and images downloaded from the internet. If you do not hold the copyright for any such item (in whole or part) that is included in your paper, please complete and return this Third

Party Rights Table: http://www.nature.com/licenceforms/snl/thirdpartyrights-origres.doc, and attach any grant of rights that you have collected.

For more information on our licence policy, please consult http://npg.nature.com/authors.